Discovery of a Dark, Massive, ALMA-only Galaxy at z ~ 5–6 in a Tiny 3 mm Survey
— **Source link** ⎋

Christina C. Williams, Ivo Labbé, Justin Spilker, Mauro Stefanon ...+7 more authors

Institutions: University of Arizona, Swinburne University of Technology, University of Texas at Austin, Leiden University
...+6 more institutions

Related papers:

- Discovery of a dark, massive, ALMA-only galaxy at z~5-6 in a tiny 3-millimeter survey

- A dominant population of optically invisible massive galaxies in the early Universe

- Galactic stellar and substellar initial mass function

- Stellar population synthesis at the resolution of 2003

- GOODS-ALMA: 1.1 mm galaxy survey - I. Source catalogue and optically dark galaxies

Discovery of a Dark, Massive, ALMA-only Galaxy at z ∼ 5–6 in a Tiny 3 mm Survey

Discovery of a Dark, Massive, ALMA-only Galaxy at $z \sim 5$–6 in a Tiny 3 mm Survey

Christina C. Williams[1,11] , Ivo Labbe[2] , Justin Spilker[3] , Mauro Stefanon[4] , Joel Leja[5,11] , Katherine Whitaker[6] ,
Rachel Bezanson[7] , Desika Narayanan[8] , Pascal Oesch[9,10] , and Benjamin Weiner[1]

[1] Steward Observatory, University of Arizona, 933 North Cherry Avenue, Tucson, AZ 85721, USA
[2] Centre for Astrophysics & Supercomputing, Swinburne University of Technology, P.O. Box 218, Hawthorn, VIC 3112, Australia
[3] Department of Astronomy, University of Texas at Austin, 2515 Speedway, Stop C1400, Austin, TX 78712, USA
[4] Leiden Observatory, Leiden University, NL-2300 RA Leiden, The Netherlands
[5] Harvard-Smithsonian Center for Astrophysics, 60 Garden St. Cambridge, MA 02138, USA
[6] Department of Physics, University of Connecticut, 2152 Hillside Road, Unit 3046, Storrs, CT 06269, USA
[7] Department of Physics and Astronomy and PITT PACC, University of Pittsburgh, Pittsburgh, PA, 15260, USA
[8] Department of Astronomy, University of Florida, 211 Bryant Space Science Center, Gainesville, FL 32611, USA
[9] Department of Astronomy, University of Geneva, 51 Ch. des Maillettes, 1290 Versoix, Switzerland
[10] International Associate, Cosmic Dawn Center (DAWN) at the Niels Bohr Institute, University of Copenhagen and DTU-Space, Technical University of Denmark,
Denmark

Abstract

We report the serendipitous detection of two 3 mm continuum sources found in deep ALMA Band 3 observations to study intermediate-redshift galaxies in the COSMOS field. One is near a foreground galaxy at $1{\farcs}3$, but is a previously unknown dust-obscured star-forming galaxy (DSFG) at probable $z_{\rm CO} = 3.329$, illustrating the risk of misidentifying shorter wavelength counterparts. The optical-to-millimeter spectral energy distribution (SED) favors a gray $\lambda^{-0.4}$ attenuation curve and results in significantly larger stellar mass and SFR compared to a Calzetti starburst law, suggesting caution when relating progenitors and descendants based on these quantities. The other source is missing from all previous optical/near-infrared/submillimeter/radio catalogs ("ALMA-only"), and remains undetected even in stacked ultradeep optical (>29.6 AB) and near-infrared (>27.9 AB) images. Using the ALMA position as a prior reveals faint signal-to-noise ratio ~ 3 measurements in stacked IRAC 3.6+4.5, ultradeep SCUBA2 850 μm, and VLA 3 GHz, indicating the source is real. The SED is robustly reproduced by a massive $M^* = 10^{10.8} M_\odot$ and $M_{\rm gas} = 10^{11} M_\odot$, highly obscured $A_V \sim 4$, star-forming SFR $\sim 300\ M_\odot\ {\rm yr}^{-1}$ galaxy at redshift $z = 5.5 \pm 1.1$. The ultrasmall 8 arcmin^2 survey area implies a large yet uncertain contribution to the cosmic star formation rate density CSFRD($z = 5$) $\sim 0.9 \times 10^{-2}\ M_\odot\ {\rm yr}^{-1}\ {\rm Mpc}^{-3}$, comparable to all ultraviolet-selected galaxies combined. These results indicate the existence of a prominent population of DSFGs at $z > 4$, below the typical detection limit of bright galaxies found in single-dish submillimeter surveys, but with larger space densities $\sim 3 \times 10^{-5}\ {\rm Mpc}^{-3}$, higher duty cycles of 50%–100%, contributing more to the CSFRD, and potentially dominating the high-mass galaxy stellar mass function.

Key words: galaxies: evolution – galaxies: high-redshift – galaxies: starburst

1. Introduction

In past decades, single-dish submillimeter surveys have identified populations of massive, dusty star-forming galaxies at $z > 1$ (e.g., Casey et al. 2014). While these galaxies are rare even at Cosmic Noon ($1 < z < 3$) when the star formation activity in the universe peaks, their contribution to the cosmic star formation rate density (CSFRD) equals that of all optical and near-infrared selected galaxies combined (Madau & Dickinson 2014). However, at $z > 3$ the situation is much less certain. A tail of submillimeter-selected galaxies have been confirmed beyond $z > 4$, but they trace only the very tip of the star formation rate (SFR) distribution at early times (e.g., Cooray et al. 2014; Strandet et al. 2017; Marrone et al. 2018). The total contribution of dust-obscured star formation, and therefore the census of star formation in the early universe, is unknown. Despite the strongly negative k-correction allowing sources to be found to $z = 10$, the overwhelming majority of (sub)millimeter-selected galaxies continue to be confirmed at $z < 3$ with Atacama Large Millimeter/submillimeter Array (ALMA) spectroscopy (Brisbin et al. 2017; Danielson et al. 2017). While some dusty galaxies have been discovered beyond $z > 5$ through gravitational lensing

(Spilker et al. 2016; Zavala et al. 2018b), the lensing correction and selection effects make it challenging to establish their contribution to the CSFRD. Progress is hampered by the limited sensitivity and low spatial resolution of single-dish submillimeter observations and the difficulty of associating detections with counterparts in the optical–near-infrared (NIR). Ultradeep SCUBA surveys over moderate ~ 100 arcmin^2 are now pushing into the range of "normal" SFRs (several 100 $M_\odot$ yr^{-1}, main-sequence galaxies; e.g., Koprowski et al. 2016; Cowie et al. 2017, 2018) and extending to $z > 4$, but the analysis is often limited by the ability to identify counterparts at other wavelengths and derive accurate redshifts.

ALMA has opened an avenue for addressing this issue through surveys at superior sensitivity and spatial resolution. ALMA deep fields at ~ 1 mm (Aravena et al. 2016; Dunlop et al. 2017) have probed to extremely deep flux limits over small areas (<5 arcmin^2). Progress has still been limited likely because dust-obscured star formation preferentially occurs in massive galaxies (Whitaker et al. 2017), which are clustered and relatively rare (~ 0.1 arcmin^{-2} at $\log(M/M_\odot) > 10.8$ and $z \sim 4$; Davidzon et al. 2017). Wider (10's arcmin^2) and shallower (~ 100–$200\ \mu$Jy) ALMA surveys at ~ 1 mm (Franco et al. 2018; Hatsukade et al. 2018) are now approaching large

---

enough areas to identify tentative massive candidates at $z > 4$ (e.g., Yamaguchi et al. 2019).

A promising development is to select at longer wavelengths (>2 mm), which optimizes the selection to dusty star formation at redshift $z > 4$ (Béthermin et al. 2015; Casey et al. 2018). However, the current state-of-the-art ALMA Spectroscopic Survey (ASPECS) at 3 mm (González-López et al. 2019), still only covered ~ 5 arcmin^2, and identified 6 continuum sources, all at $z < 3$. Larger archival studies of ALMA 3 mm observations to find high-redshift candidates report some spectroscopic confirmations, but like the 1 mm redshift distribution, the majority lie at $z < 3$ (Zavala et al. 2018a). Recent advances with IRAM/GISMO provide evidence that 2 mm surveys favor selecting higher-redshift sources (Magnelli et al. 2019), although counterpart identification continues to be problematic due to large beam sizes. Overall, the number of strong candidates for dust-obscured sources at $z > 4$ remains small and as a result, the contribution of dust-obscured star formation in the early universe is poorly constrained.

Here we report the serendipitous discovery of 2 previously unknown sources in deep ALMA 3 mm observations in the COSMOS field, and assess the implications for dust-obscured star formation at $z > 3$. We assume a ΛCDM cosmology with $H_0 = 70$ km s^{-1} Mpc^{-1}, $\Omega_M = 0.3$, $\Omega_\Lambda = 0.7$, and a Kroupa (2001) initial mass function (IMF).

2. Methods

2.1. ALMA Millimeter Interferometry

The ALMA observations are part of a program targeting CO(2-1) line emission in $z \sim 1.5$ galaxies (2018.1.01739.S, PI: Williams; 2015.1.00853.S, PI: Bezanson) in the COSMOS field. The data presented here include ALMA maps of five galaxies, and results on these targets are presented elsewhere (Bezanson et al. 2019; C. C. Williams et al. 2019, in preparation). In one of these pointings we identified two serendipitous continuum sources, unrelated to the original target, which we will now describe in detail.

ALMA Band 3 observations were carried out in two observing blocks on 2018 December 23 and 24 under program 2018.1.01739.S (PI: Williams). One 1.875 GHz spectral window was centered at the sky frequency (94.92 GHz) with 7.8 MHz (~ 24 km s^{-1}) channelization. Three additional 1.875 GHz bandwidth spectral windows were placed at sky frequencies 96.8, 106.9, and 108.8 GHz for continuum observations, each with 15.6 MHz channelization. A total of 43 antennas were active, reaching maximum baselines of 500 m, for an angular resolution of ~ 2 arcsec (synthesized beam major axis = $2\rlap{.}{''}2$, minor axis = $1\rlap{.}{''}7$ under natural weighting). The total time on-source was 97 minutes.

The data were reduced using the standard ALMA Cycle 6 pipeline, and no problems with the pipeline calibration were found. The imaged data reach a continuum sensitivity of 5.7 μJy/beam at 101.9 GHz, and a typical line sensitivity of 55–65 μJy/beam per 100 km s^{-1} channel. We imaged the data using natural weighting, creating a 101 GHz continuum image of the field from all four spectral windows. We imaged the data using $0\rlap{.}{''}2$ pixels and created a 500×500 pixel image, yielding images $100''$ on a side. Given the ALMA primary beam at this frequency ($\sim 57''$ FWHM), these images extend to approximately the 0.05 response point of the primary beam.

2.2. ALMA Source Detection

Interferometric maps without correction for the primary beam response have uniform, normally distributed noise properties across the field, and source detection significance is straightforward to measure from such maps. Two blind 3 mm continuum sources were apparent in this map, located $24\rlap{.}{''}6$ and $38\rlap{.}{''}2$ from the phase center, corresponding to primary beam response levels of 0.57 and 0.29, respectively. Each source is detected at a peak signal-to-noise ratio (S/N) of ~ 8; the probability of finding a Gaussian noise fluctuation of this magnitude given the number of independent beams in the images is exceedingly low ($< 10^{-9}$). Both sources thus are real. The 3 mm flux densities of these sources, corrected for the primary beam response, are 155 ± 20 μJy and 75 ± 10, hereafter referred to as 3MM-1 and 3MM-2, respectively. Neither source is spatially resolved, based on a comparison of the peak pixel values and the integrated flux densities.

After finding both continuum sources in the combined map, we reimaged the upper and lower sidebands of the data separately in order to determine the spectral index of each source at these frequencies. Thermal dust emission on the Rayleigh–Jeans tail has a very steep power-law index with $S_\nu \propto \nu^{2+\beta}$ and $\beta \sim 1.5$–2, while non-thermal synchrotron emission typically exhibits a negative spectral index, $S_\nu \propto \nu^{-0.8}$. Given their respective frequencies, we expect dust emission to be $\sim 50\%$–60% brighter in the upper sideband than in the lower sideband. We find spectral indices for both continuum sources in excellent agreement with the expectation for thermal dust emission.

We also reimaged the data of both sidebands to search for blindly detected emission lines in each of the two continuum sources, using channel widths ranging from 100 to 400 km s^{-1}. 3MM-2 contains a serendipitous emission line centered at 106.5 GHz, with an integrated flux density of 0.66 ± 0.1 Jy km s^{-1}. The spectrum is shown in Figure 2. A Gaussian fit indicates a width of 630 ± 70 km s^{-1}. Assuming the line is a transition of carbon monoxide, the possible redshifts are $z = [0.08, 1.16, 2.25, 3.33, 4.41, 5.49]$. We find no significant emission lines in the spectrum of 3MM-1, and no evidence for a line at the same frequency of 3MM-2. A Gaussian fit restricted to the same frequency and width results in an integrated flux density of 0.17 ± 0.2 Jy km s^{-1}, indicating no evidence for a line at that location.

Both 3MM-1 and 3MM-2 were also contained within the field of view of an additional ALMA Band 3 program, 2015.1.00861.S. Both sources were again far out in the primary beam of these data, at approximately the 0.25 and 0.1 response points, respectively. These data are described in more detail in Silverman et al. (2018), and have non-overlapping frequency coverage with our own data. We downloaded and imaged these data following the same procedure as for our own data. The new images reach a continuum sensitivity at a phase center of 10 μJy/beam at 93.5 GHz and a line sensitivity of 120–170 μJy/beam per 100 km s^{-1} channel, approximately a factor of two higher than that in our data. Neither source is detected in the continuum in these data, nor was expected to be detected given the sensitivity, effective frequency, and position of our sources within the ALMA primary beam. We additionally searched these data for blindly detected CO lines as in our own data, but found no significant emission lines. The limited (primary beam-corrected) sensitivity of these data
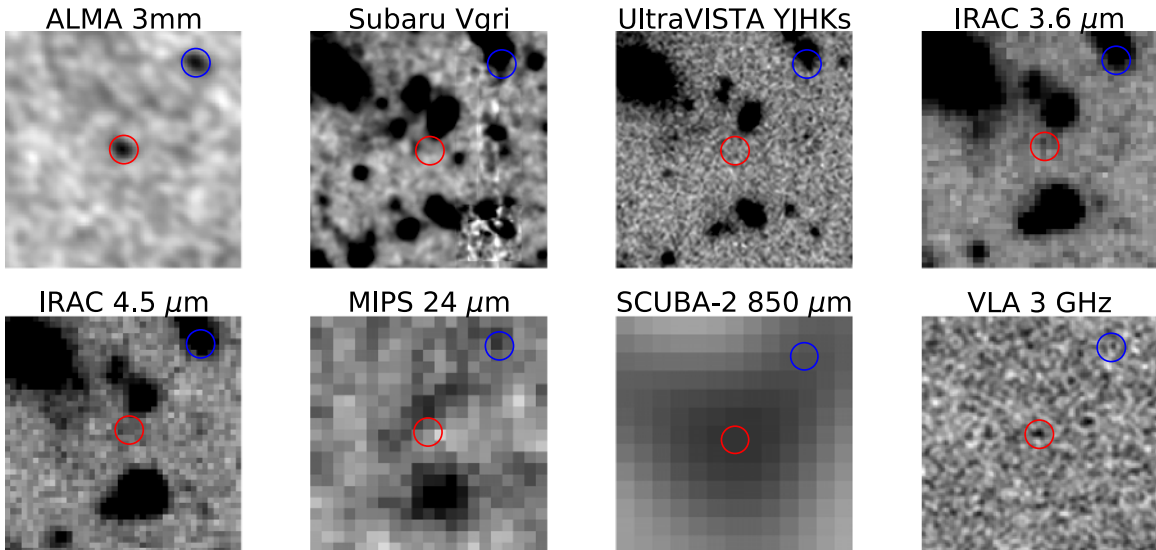
Figure 1. Cutouts ($25'' \times 25''$) centered at a 3 mm position of 3*MM*-1 (red circle; $3''$ diameter). 3*MM*-1 was not previously detected ($>3\sigma$) at any shorter wavelength, including deep optical and near-IR stacks, *Spitzer*, *Herschel*, and S2COSMOS SCUBA2 850 μm. Remeasuring with the ALMA position as a prior reveals marginal 2σ–3σ measurements in IRAC 3.6+4.5 and 850 μm, consistent with heavy dust obscuration at $z > 4$. It is faintly detected at 3 GHz (4σ), indicative of a moderate radio excess due to a possible active galactic nucleus (AGN). The 1.4 GHz image is excluded because neither source is significantly detected. 3*MM*-2 is also identified (blue circle), and is blended with a foreground galaxy at $z = 0''95$, $1''3$ north (Muzzin et al. 2013; Laigle et al. 2016).

preclude us from drawing strong conclusions about the redshifts of either source.

For convenience, we define an equivalent survey area as the total area across all five ALMA maps at which a source with the same $S_{3\,\mathrm{mm}}$ as 3*MM*-1 would be detected at $>5\sigma$. Taking into account the small variations in the central frequency of each map (tuned to the specific redshift of the target $z \sim 1.5$ galaxies), which change the primary beam response shape and the detection threshold (25–31 μJy) due to the steep spectral index of dust emission, we derive a total survey area of 8.0 arcmin^2 to 155 μJy (5σ limit).

2.3. Multiwavelength Photometry

3*MM*-1 has extremely deep coverage at all optical-to-submillimeter wavelengths, yet it has no counterpart within a radius of $3''3$ in the deepest published multiwavelength catalogs in COSMOS to date, from 0.6 to 1100 μm (Le Floc'h et al. 2009; Aretxaga et al. 2011; Muzzin et al. 2013; Laigle et al. 2016; Geach et al. 2017; Hurley et al. 2017) or 3–1.4 GHz (Schinnerer et al. 2010; Smolčić et al. 2017). The astrometry of multiwavelength catalogs in COSMOS are excellent owing to the registration between VLA observations (e.g., Schinnerer et al. 2007), ground-based optical and space-based facilities, with an astrometric accuracy of 5 mas (Koekemoer et al. 2007). Similar astrometric accuracy was found between ALMA and COSMOS multiwavelength data sets (Schreiber et al. 2017). There is no apparent flux at optical-to-*Spitzer*/IRAC wavelengths at the ALMA position (Figure 1). 3*MM*-2 is also missing from these catalogs, likely because it is blended with a bright neighboring galaxy $\sim 1''3$ to its north, with a photometric redshift 0.95 (see Figure 1), but appears detected in *Ks* and IRAC. It is possible that the ALMA source is simply a highly obscured region in the low-redshift galaxy, which can be ruled out by spatially deblended SED analysis. We therefore proceeded to perform deblended photometry on both ALMA positions using the following data sets.

2.3.1. Optical, Near-infrared, and Spitzer/IRAC

The optical data consist of the Subaru/Suprime-cam B_j, V_j, g^+, r^+, i^+ and z^+-imaging (Taniguchi et al. 2007), with 5σ limits of $\sim$25–27.4 mag in $1''2$ apertures, and Subaru HyperSuprimeCam (HSC) g, r, i, z, and y (Aihara et al. 2018a, 2018b) imaging ($\sim$25–26.8 mag, 5σ). Ultradeep NIR coverage is provided by the 4th data release of the UltraVISTA survey (McCracken et al. 2012), thanks to mosaics in the Y, J, H, and K_s filters to $\sim$25 mag (AB, 5σ). Remarkably, the coverage in the K_s band from DR4 is $\sim$0.9 mag deeper than that from DR3, allowing us to place strong constraints on the flux density of 3*MM*-1 at NIR wavelengths. Stacked images were constructed using the optical imaging 0.4–0.8 μm and the NIR imaging 0.9–1.6 μm. We use *Spitzer*/IRAC 3.6 μm and 4.5 μm mosaics that combine data from the S-COSMOS (Sanders et al. 2007) and the *Spitzer* Large Area Survey with HSC (SPLASH, PI: Capak) programs ($\sim$24.5 mag, 5σ in $1''8$ apertures), and the 5.8 μm and 8.0 μm from the S-COSMOS program ($\sim$20.7 mag, 5σ in $1''8$ apertures).

We measured flux densities for 3*MM*-1 in the optical and UltraVISTA bands in $1''2$-diameter apertures after subtracting the neighbors using MOPHONGO (Labbé et al. 2013, 2015). This procedure carefully models the light profiles of the sources using a higher-resolution image as a prior, minimizing potential contamination by bright nearby objects (see Figure 3). In our analysis we adopted the HSC z-band image as a prior for 3*MM*-1, as it provides the best compromise between depth and resolution and the F814W-band image for 3*MM*-2, given the nearby bright neighbor at $\sim 1''3$ distance. Because of the broader PSF, we adopted $1''8$ apertures for our estimates in the IRAC bands. Total flux densities were then estimated from the spatial profile and the relevant PSF-correction kernel.

2.3.2. Far-infrared to Submillimeter

Far-infrared and submillimeter *Herschel* fluxes were measured for both galaxies by simultaneously fitting Gaussian
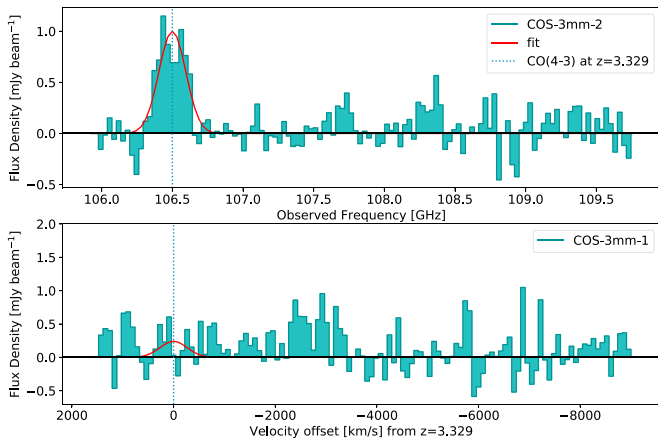
Figure 2. Portion of the observed ALMA Band 3 spectrum covering the detected CO line in 3*MM*-2 at 106.5 GHz (upper sideband). The CO solution corresponding to CO(4-3) at $z = 3.329$ is in excellent agreement with the photometric redshift measured in Section 2.4. The line flux is 0.66 ± 0.1 Jy km s^{-1} and a Gaussian fit produces a width of 650 km s^{-1}. No line is found at the same frequency in the spectrum of 3*MM*-1 (lower panel) with formal SNR = 0.8. No lines are detected in the lower sideband from $94 < \nu < 96.8$ GHz.

profiles at fixed prior locations in the *Herschel* images specified by the ALMA locations and augmented by the MIPS positions of all neighboring objects from the S-COSMOS data (Sanders et al. 2007; Le Floc'h et al. 2009). The FWHMs of the Gaussians were 7.″7, 12″ (PACS 100, 160 μm) and 18, 25, and 37′ (SPIRE 250, 350, 500 μm), respectively. Uncertainties were computed by fitting Gaussians at random locations within a 2 arcmin radius and computing the rms. Flux calibration was performed by comparing to the 24 μm prior catalog of *Herschel* DR4 (Oliver et al. 2012; Hurley et al. 2017). Comparison of the measured SPIRE fluxes with those published showed a scatter of 30%; this was added in quadrature to the flux uncertainties for those bands. The correction is minor considering the S/N of $\lesssim 1$ of the SPIRE fluxes. For SPIRE 500 μm only, the flux of a neighboring $z_{\rm spec} = 1.45$ galaxy 5″ to the south was subtracted separately prior to deblending, using its predicted IR emission based on the infrared SED of Wuyts et al. (2011) and its $\rm SFR_{24,IR} = 65\ M_\odot\ yr^{-1}$.

The procedure for measuring photometry at 850 μm follows that of *Herschel*/PACS and SPIRE (250 and 350 μm) using the ALMA and MIPS positions as priors. The sources lie in a region of shallower ($\sigma_{850} \sim 3$ mJy/beam) coverage in the inhomogeneous SCUBA-2 Cosmology Legacy Survey (S2CLS; Geach et al. 2017) and are undetected in this map. We therefore use the state-of-the-art S2COSMOS observations, which achieved a $\sigma_{850} \sim 1.2$ mJy over the entire field (Simpson et al. 2019).

2.3.3. Radio VLA 3GHz and 1.4 GHz

Neither source has a counterpart in either the VLA 3 GHz 5σ source catalog (Smolčić et al. 2017) or the 1.4 GHz deep survey 5σ source catalog (Schinnerer et al. 2010). Photometry on the 3 GHz map using the ALMA position as a prior reveals a $9.98 \pm 2.39\ \mu$Jy/beam (4σ) point source for 3*MM*-1, below the detection limit of the Smolčić et al. (2017) catalog. Blindly detected sources at this flux density have a high probability ($>50\%$) of being spurious (Smolčić et al. 2017), therefore requiring the ALMA prior in order to be considered real. 3*MM*-2 shows no significant flux to 3σ limits of $\sim 7\ \mu$Jy/beam. Within

10 arcmin^2, the 1.4 GHz map has an rms of $\sim 17\ \mu$Jy/beam and no significant flux ($>3\sigma$) is detected from either galaxy.

2.4. SED Modeling

The deep photometry from $\lambda = 0.4$–3000 μm places strong constraints on the SEDs and allows us to model their stellar populations and redshift. It should be noted that even if a source is not formally detected ($>3\sigma$) at most wavelengths, the absence of flux can still provide useful constraints, in particular on the redshift. All fitting is performed in linear fluxes and uncertainties and no upper limits are enforced on measurements with low S/Ns.

We use the Bayesian Analysis of Galaxies for Physical Inference and Parameter EStimation (BAGPIPES) code (Carnall et al. 2018), which assumes the stellar population synthesis models of Bruzual & Charlot (2003) and implements nebular emission lines following the methodology of Byler et al. (2017) using the CLOUDY photoionization code (Ferland et al. 2017). We select the flexible dust absorption model of Charlot & Fall (2000), with the exponent of the effective absorption $\propto \lambda^{-n}$ as a free parameter and adopt the Draine & Li (2007) dust emission model under the assumption of energy balance, such that dust-absorbed light is re-radiated in the far-infrared. All stellar populations have this effective absorption, while the youngest stars (defined as those with age <10 Myr) have an extra factor of attenuation applied (η) to account for dusty birthclouds.

The dust emission model is parameterized using the starlight intensity U incident on the dust (translating into a distribution of dust temperatures), the amount of PAH emission, and the fraction of dust at the coldest temperature. We further assume a delayed exponential star formation history with τ and age left free and metallicities ranging from 0.2 to 2.5$Z_\odot$. For each parameter, uniform, diffuse priors are assumed (see Table 1). In general, we do not expect to constrain most free parameters, but we will marginalize over those and limit the discussion to the more important parameters including redshift, stellar mass, and SFR. Where relevant, we will also quote results based on assumptions often used in the literature, such as assuming a fixed Calzetti et al. (2000) dust attenuation model.

3. Results

The photometry for both galaxies is presented in the Appendix (Table 2).

3.1. 3MM-1

3*MM*-1 is undetected ($<3\sigma$) in individual optical (>27AB), near-infrared (>25.2), and *Spitzer*/IRAC (>25.2) bands, and remains undetected in the stacked ultradeep optical (>29.6 AB) and near-IR (>27.9 AB) data (1σ limits). The source is faintly detected (25.2 AB $\sim 3\sigma$) in deep stacked IRAC 3.6+4.5 observations, indicating the source is likely real with extremely red colors. Owing to the shallower depth, the source is undetected in deep *Spitzer*/MIPS 24 μm and *Herschel* PACS +SPIRE 160–500 μm. The flux measured with SCUBA is $S_{850} = 3.5 \pm 1.1$ mJy (SNR = 3.1). This flux density is fainter than the depth typically achieved by deep single-dish submillimeter surveys (>3.5–5 mJy; e.g., Weiß et al. 2009; Aretxaga et al. 2011; Cowie et al. 2017; Geach et al. 2017) at robust detection thresholds ($\gtrsim 4\sigma$). The observed SED is shown in Figure 4 (left panel). For clarity, photometry with S/N < 1 is indicated with arrows at the 1σ rms level, and
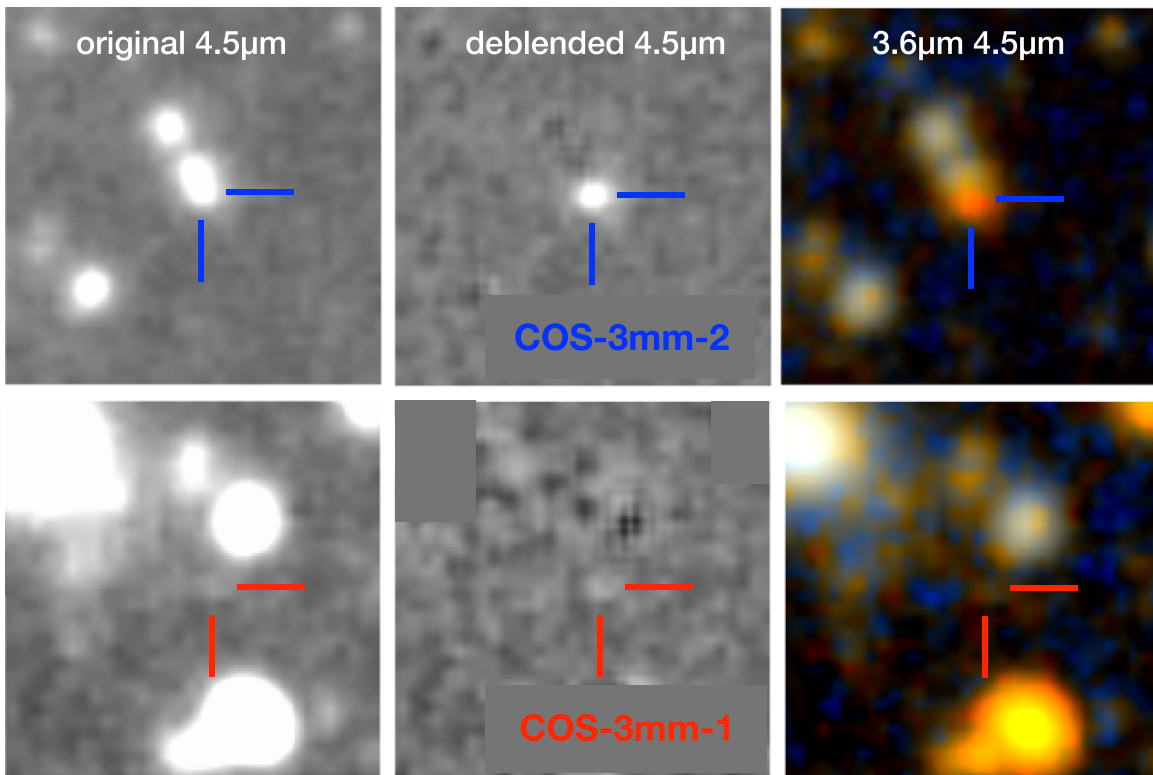
Figure 3. Illustration of the deblending procedure using the MOPHONGO software (Labbé et al. 2015). Deblending is performed by simultaneously fitting the pixels of all sources using the deep optical images and the ALMA positions as priors and accounting for differences in the PSFs. Top row: deblending results for the 4.5 μm band centered on the ALMA position of 3MM-2 (12″ × 12″). The left panel shows the original 4.5 μm image, the middle panel shows 3MM-2 after other modeled sources have been subtracted, and the right panel shows a 3.6–4.5 μm color image clearly indicating a vastly different IRAC color at the location of the ALMA source. Bottom row: higher contrast, zoomed-in panels centered on the ALMA position of 3MM-1, showing a faint AB ∼ 25.2 IRAC source after subtracting the PSF wings of a bright foreground neighbor.

S/N > 1 with 1σ error bars. The deep non-detections at all wavelengths between 24 and 500 μm and the extreme flux ratios ($S_{24}/S_{850} < 4 \times 10^{-3}$, $S_{24}/S_{3\,mm} < 9 \times 10^{-2}$, $S_{4.5}/S_{850} < 9 \times 10^{-5}$, $S_{4.5}/S_{3\,mm} < 2 \times 10^{-3}$; see, e.g., Cowie et al. 2018; Yamaguchi et al. 2019) demand that the dust peak be highly redshifted, $z > 4$.

Fitting stellar population models, we find the observations are well reproduced by a massive $10^{10.8 \pm 0.4} M_{\odot}$, star-forming SFR $= 309^{+241}_{-149} M_{\odot}\,yr^{-1}$, highly obscured $A_V \sim 4^{+1.4}_{-1.0}$ galaxy at very high redshift $z \sim 5.5^{+1.2}_{-1.1}$. The SED-fitting results are shown in Figure 4 and the posterior values and priors are listed in Table 1. The posterior distributions of all parameters are presented in Figure 7. Adopting a classical Calzetti dust law would increase the stellar mass, SFR, and redshift by 60%, 10%, and 5%, respectively. These changes are within the uncertainties, so we elect to adopt our more conservative values measured assuming Charlot & Fall (2000) as fiducial. We also experimented with fitting only the mid-infrared to submillimeter SED, finding the same results. In all cases, the solutions require the galaxy to be at high redshift, with $z > 4.1$ at 90% confidence and a total infrared luminosity $L_{IR} = 4 \times 10^{12} L_{\odot}$ (based on integrating the median posterior spectrum). Adopting an SED typical for the most obscured $A_V > 3.5$ SMGs (da Cunha et al. 2015) produces similar redshift and L_{IR}, as does adopting the Arp 220 SED. Converting to SFR using the Kennicutt & Evans (2012) conversion, which does not implicitly assume a SFH, results in a larger estimated SFR $= 540 M_{\odot}\,yr^{-1}$, but consistent within the 1σ uncertainties from SED fitting.

Calculating redshift using the radio-to-submillimeter spectral index method (using 850 μm and the upper limit on 1.4 GHz) implies a lower limit to the photometric redshift of ∼4.7 (e.g., Carilli & Yun 1999). We note that this is very similar to the massive dusty galaxy HDF850.1, which had a redshift 4.1 according to this relation (Dunlop et al. 2004), and was later spectroscopically confirmed at $z = 5.2$ (Walter et al. 2012). The SED of 3MM-1 is very similar to that of HDF850.1; scaling its best-fit SED to the 850 μm and 3 mm fluxes of 3MM-1 predicts its observed 3 GHz radio flux of 10 μm (Figure 5).

The observed 3 GHz radio flux (4σ) is in excess of that expected from empirical SED templates for obscured star-forming galaxies (e.g., SMGs; da Cunha et al. 2015) and recent calibrations of the redshift-dependent ratio of total infrared luminosity to rest-frame 1.4 GHz luminosity density (Delhaize et al. 2017; Tisanić et al. 2019). For typical assumptions of the radio spectral slope $S_\nu \propto \nu^{-0.8}$ (dashed line in Figure 4), the radio emission of 3MM-1 is a factor of ∼6 ± 1.5 higher than expectations for star formation, in excess of the commonly adopted ×3 threshold for AGN activity (Daddi et al. 2009). No evidence for redshift evolution in the spectral slope, or dependence on sSFR or distance from the main sequence has been reported (Magnelli et al. 2015).

The radio excess therefore indicates plausible evidence for the presence of an AGN. We note that no X-ray counterpart exists within 5″ (Civano et al. 2016), although this is not surprising given the high redshift of 3MM-1. Given the possible presence of an AGN, it is worth noting that inferred parameters

Table 1
Stellar Population Properties of 3 mm Continuum Sources

| Parameter | 3*MM*-1[a] | 3*MM*-2 | 3*MM*-2 | Range (Uniform Prior) |
Attenuation Curve	CF00	CF00	Calzetti	
Coordinates	$10{:}02{:}36.82 + 02{:}08{:}40.60$	$10{:}02{:}36.30 + 2{:}08{:}49.55$		
Redshift	$5.5^{+1.2}_{-1.1}$	$z_{CO} = 3.329$	$z_{CO} = 3.329$	(0.0, 10.0)
SFR [$M_\odot$ yr^{-1}]	309^{+241}_{-149}	247^{+77}_{-76}	112^{+27}_{-38}	
Log$_{10}$ Stellar Mass [$M_\odot$]	$10.8^{+0.4}_{-0.4}$	$11.1^{+0.2}_{-0.2}$	$10.2^{+0.2}_{-0.2}$	(6.0, 14.0)
Mass-weighted age [Gyr]	$0.2^{+0.1}_{-0.1}$	$0.5^{+0.1}_{-0.2}$	$0.1^{+0.2}_{-0.1}$	
A_V	$4.0^{+1.4}_{-1.0}$	$2.7^{+0.3}_{-0.3}$	$1.4^{+0.1}_{-0.1}$	(0.0, 10.0)
η[b]	$2.0^{+0.6}_{-0.6}$	$2.1^{+0.6}_{-0.8}$	$2.5^{+0.3}_{-0.5}$	(1, 3.0)
Umin[c]	$13.0^{+7.7}_{-7.3}$	$7.6^{+6.3}_{-4.0}$	$4.8^{+3.4}_{-2.4}$	(1, 25.0)
gamma[d]	$0.5^{+0.3}_{-0.3}$	$0.5^{+0.3}_{-0.3}$	$0.5^{+0.3}_{-0.3}$	(0.01, 0.99)
n[e]	$0.9^{+0.6}_{-0.4}$	$0.4^{+0.1}_{-0.1}$	…	(0.1, 2.0)
qpah[f]	$2.3^{+1.1}_{-1.1}$	$3.3^{+0.5}_{-1.0}$	$3.0^{+0.7}_{-1.1}$	(0.5, 4.0)
Log$_{10}$ L_{IR}[g] [$L_\odot$]	12.6	12.4	12.1	
Gas mass [$M_\odot$]	$0.5\text{–}1.5 \times 10^{11}$	$4\text{–}9 \times 10^{10}$		

Notes.
[a] Fitting priors are uniform with the range as defined in the last column.
[b] Multiplicative factor producing extra attenuation for young stars.
[c] Starlight intensity on dust grains, related to dust temperature as $T_{dust} \propto U^{1/6}$ (Draine & Li 2007).
[d] Fraction of stars at Umin.
[e] Power-law slope of the dust extinction law (for Charlot & Fall 2000).
[f] PAH mass fraction.
[g] Total infrared luminosity (8–1000 μm) in units from integrating the median posterior spectrum in Figure 4.

from SED fitting could be biased by AGN emission, in particular in the mid-infrared (e.g., Leja et al. 2018). Therefore, we investigate any possible contamination using the empirical AGN-dominated template published by Kirkpatrick et al. (2015). We use their mid-infrared template based on galaxies with the largest mid-infrared luminosity contribution from AGN emission scaled to the 24 μm flux of 3*MM*-1 and subtract the predicted AGN contribution from the observed SED. This represents the maximum AGN contribution that could be accommodated by the data without violating the observed photometry. We then remeasure the SED fitted parameters. Subtracting this empirical AGN template reduces the SFR by ∼15%, well within the uncertainty, but does not change the inferred stellar mass significantly. We conclude that any AGN contribution does not significantly impact our SED-fitting results.

Finally, the 3 mm flux density enables an estimate of the molecular gas mass for 3*MM*-1 following the calibration of submillimeter flux to gas mass (Scoville et al. 2016). Exploring the range of the photometric redshift PDF, and typical assumptions about the dust emissivity, temperature, and dust-to-gas ratio, we find that 3*MM*-1 likely has $M_{gas} \sim (0.5\text{–}1.5) \times 10^{11}$ $M_\odot$. This is independent evidence that the galaxy is massive, with a high inferred gas fraction (∼60%).

3.2. 3MM-2

3*MM*-2 is optically faint, but detected in $K_{s,AB} = 24.2$ and relatively bright in IRAC ∼23 mag, with red optical-to-IRAC colors. There is an apparent break between the J_s and H-band, consistent with a Balmer/4000 Å break at $z \sim 3$. The source is undetected at 24–870 μm, but with less extreme flux ratios ($S_{24}/S_{3\,mm} < 3.5 \times 10^{-1}$, $S_{4.5}/S_{3\,mm} < 3 \times 10^{-2}$) compared to 3*MM*-1, indicating a lower redshift.

We follow the same procedure as before to fit the SED, finding a well-constrained photometric redshift of $z = 3.3 \pm 0.2$ (99% probability between $2.7 < z < 3.7$), ruling out that this source is simply a highly obscured region in the nearby $z = 0.95$ foreground galaxy to the north. Considering the CO emission line detection (consistent with redshifts 2.25, 3.33, and 4.41), we determine the line is likely CO(4–3) at $z = 3.329$, in agreement with the best-fit photometric redshift. Fixing the redshift to the spectroscopic redshift, the observations are best reproduced with a massive $10^{11.1} M_\odot$, star-forming SFR = 250 $M_\odot$ yr^{-1}, highly obscured $A_V \sim 2.7$ galaxy. Using the Kennicutt (1998), Kennicutt & Evans (2012) conversion from L_{IR} to SFR yields ∼375 $M_\odot$ yr^{-1}. The derived gas mass using the CO(4-3) line flux (assuming the average CO excitation from Bothwell et al. 2013) is in the range ∼(1–4) × 10^{11} $M_\odot$, given the factor of four scatter in measured excitation for high-redshift dust-obscured galaxies (e.g., Figure 1 in Narayanan & Krumholz 2014). The 3 mm derived gas mass is (4–9) × 10^{10} $M_\odot$. Both estimates indicate gas fractions in the range 30%–70%. The SED properties for 3*MM*-2 are listed in Table 1, the SED fit is shown in Figure 4, and posterior distributions for the parameters are presented in Figure 8.

The best-fit power-law index for the Charlot & Fall (2000) dust model is $n = 0.4 \pm 0.1$, flatter than the $n = 0.7$ appropriate for typical nearby starburst galaxies. The flat spectral index means that the attenuation curve is "grayer" than a Calzetti attenuation law (e.g., Chevallard et al. 2013), resulting in larger attenuation for the same amount of reddening $E(B - V) = 0.3$. The assumed attenuation model can have a large impact on the derived stellar mass. If instead of a flexible attenuation model a classical Calzetti starburst law is assumed then the fits result in a factor $8^{+7.1}_{-3.9}$ lower stellar mass ($10^{10.2}$ $M_\odot$) and factor $2.2 \pm 0.7\times$ lower SFR (same answer if the infrared-to-millimeter constraints are also removed). The large difference in stellar mass is remarkable. The reason is that
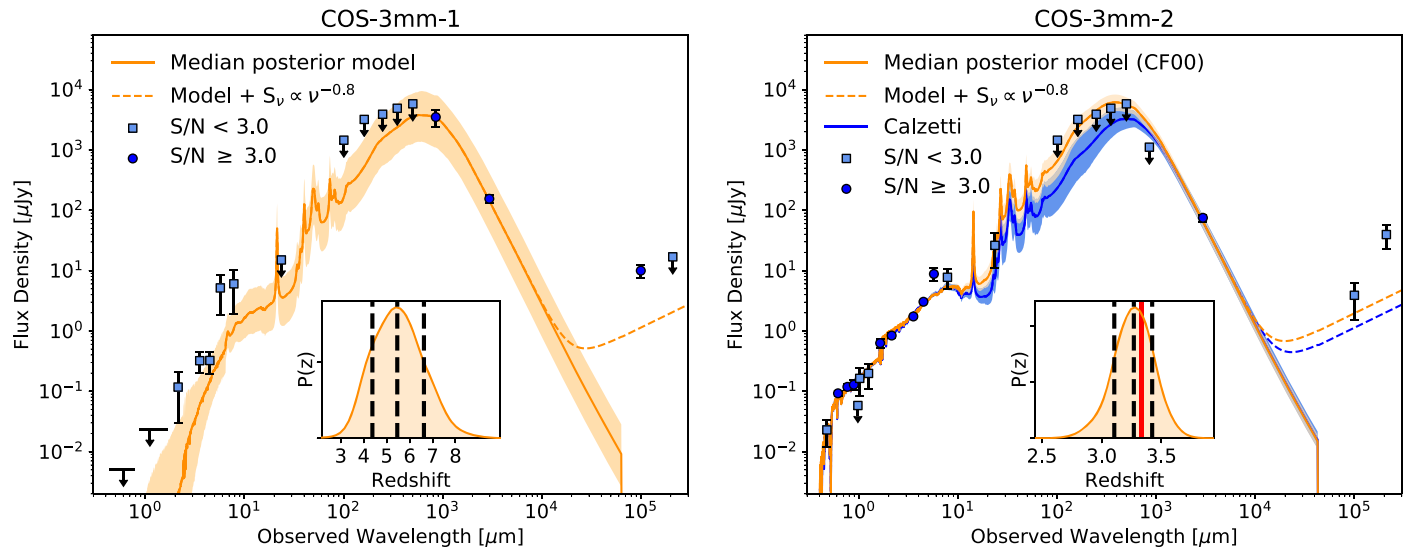
Figure 4. Left: observed photometry of 3*MM*-1 (points). For display purposes, we show 1σ upper limits (downward arrows) for data with S/N < 1 and stacked optical and NIR fluxes (horizontal bars) instead of the individual optical/NIR non-detections. Any photometry with SNR > 1 is plotted with 1σ uncertainties but does not necessarily indicate a significant detection. The light blue squares indicate photometry with S/N < 3, and the dark blue circles indicate detections with S/N ⩾ 3. Shown are the median posterior spectrum (dark orange) and 16–84th percentile range (light orange) from Bayesian SED fitting with BAGPIPES assuming the Charlot & Fall (2000) dust model. Insets contain the posterior redshift distribution and the 16, 50, and 84th percentiles (black lines). The deep FIR photometric limits at 24 < λ < 250 μm favor high redshift (90% probability at z > 4.1). The dotted line indicates the radio spectrum ∝ ν^{−0.8} expected from the total L_{IR} (Tisanić et al. 2019), suggesting a 3 GHz radio excess. Right: SED of 3*MM*-2. As in the left panel, all photometry with S/N > 1 are plotted as error bars with 1σ uncertainties. The photometric redshift agrees with CO(4–3) at z_{CO} = 3.329 (red line). The SED fit (orange) assumes the Charlot & Fall (2000) dust model and the redshift is fixed to z_{CO}. Also shown is a fit assuming a Calzetti et al. (2000) starburst attenuation law (blue curve), a common assumption in high-redshift studies that can drastically change the estimated stellar mass, L_{IR}, and SFR. The blue curve has a 8× lower stellar mass and 2× lower SFR while still adequately fitting the observations.

the steeper reddening curve of Calzetti reproduces the data with an intrinsically blue, young, low *M/L* ratio stellar population, driving the lower masses. The Charlot & Fall (2000) model requires an older, redder, higher *M/L* population, while also implying larger attenuation at all wavelengths, including the near-infrared. We note that these results all assume energy balance and a parametric delayed–τ SFH. We explore the dependence on SFH by also fitting the SED with PROSPECTOR (Leja et al. 2017), which is capable of fitting a non-parametric SFH in logarithmic bins of age (Leja et al. 2019). These fits produce qualitatively similar results, with Calzetti yielding ∼2× lower SFR and stellar mass.

An independent estimate of mass can be derived by estimating the dynamical mass from the 630 km s^{-1} width of the CO emission line at 106.5 GHz (Figure 2). Following the procedure used by Wang et al. (2013), we compute $V_{circ} = 0.75$FWHM(CO)$/\sin(i)$ and $M_{dyn} = 1.16 \times 10^5 V_{circ}^2 D$, where we note that inclination angle i and disk diameter D (in kpc) are unknown. Adopting the mean size $R_e = 3^{+1.8}_{-0.9}$ kpc expected for massive $10^{11} M_\odot$ star-forming galaxies at $z = 3$ (van der Wel et al. 2014), we find $M_{dyn} \sin^2(i) = 1.5^{+1.0}_{-0.5} \times 10^{11} M_\odot$. Assuming a disk geometry with an inclination angle of $i = 45°$ would imply $M_{dyn} \sim 3 \times 10^{11} M_\odot$. Overall, the high dynamical mass appears to agree better with the high stellar mass inferred from the Charlot & Fall (2000) dust model with a flat n than with the Calzetti-based stellar mass, but the large uncertainties in dynamical and stellar mass prevent firmer conclusions.

3.3. Redshifts

Given the close $r \sim 15''$ separation on the sky of the two ALMA sources we consider the possibility that they are at the same redshift. The redshift of 3*MM*-2 ($z = 3.329$) is strongly disfavored for 3*MM*-1 (1% probability $z < 3.3$). Alternatively,

our identification of $z_{CO(4–3)} = 3.329$ for 3*MM*-2 is erroneous and the galaxy is at $z_{CO(5–4)} = 4.41$, more consistent with 3*MM*-1. This is unlikely based on the SED fit of 3*MM*-2, which is well constrained by the presence of both a Lyman Break and Balmer break. We find no significant emission line (S/N > 3) in the spectrum of 3*MM*-1, which suggests it is unlikely at $3.20 < z < 3.35$ and $3.72 < z < 3.90$. A Gaussian fit to the spectrum of 3*MM*-1 at fixed 106.5 GHz indicates SNR = 0.8, providing no evidence for 3*MM*-1 and 3*MM*-2 occupying the same dark matter halo (DMH). Additionally, we scan the nearby velocity space in case both galaxies are in a large-scale structure filament, but we find no emission line of S/N > 2 within $\Delta v = \pm 2000$ km s^{-1}. Finally, we consider the odds of finding two 3 mm sources within $r \sim 15''$ on the sky. Using the 3 mm number counts of Zavala et al. (2018a), we simulate uniformly random distributions of two sources, which indicate a ∼10% chance of finding a 75 μJy source within $r < 15''$ of a 155 μJy source. These odds are low, but not negligible. Overall, there is no conclusive evidence that the two sources are at the same redshift. We therefore proceed and take the $z_{phot} = 5.5 \pm 1.1$ for 3*MM*-1 at face value.

4. Discussion

4.1. Implications from Full Optical-to-millimeter Spectrum SED Fitting

We consider the SED-fitting analysis using a stellar population model with self-consistent dust absorption and emission under the assumption of energy balance and constrained by high-quality optical-to-millimeter observations. In the case of the $z \sim 5.5$ source 3*MM*-1, which lacks strong detections at any wavelength other than 3 mm, it is remarkable that the Bayesian posterior probability distributions for key parameters such as redshift, stellar mass, dust attenuation, and

SFR are as constrained as they are (see Table 1 and Figure 7). Closer inspection indicates that the results are mostly driven by the combination of the high S/N ALMA measurement with deep photometric limits in the short-wavelength infrared (*Spitzer*/MIPS and *Herschel*/PACS 100–160 μm), which demand that the dust emission peak is highly redshifted ($z > 4$) and the SFR is high. It is likely that the uncertainties on the stellar mass and other stellar population parameters are underestimated, because of the tight prior imposed by the parametric SFH (Carnall et al. 2019; Leja et al. 2019). We note that our choice of a rising SFH produces a relatively conservative (lower) estimate of stellar mass compared to constant or declining SFH.

There is accumulating evidence that the attenuation law in very dusty galaxies can be flatter than the Calzetti law (Salmon et al. 2016; Leja et al. 2017; Salim et al. 2018), possibly caused by a more uniformly mixed geometry of both old and young stars with dust (Narayanan et al. 2018). The flat inferred attenuation law $\lambda^{-0.4}$ for 3*MM*-2 is not surprising in that regard. It is notable and sobering, however, that modeling the optical-to-millimeter with a classical Calzetti starburst law instead (keeping everything else the same) results in significantly lower SFR and stellar mass ($10^{10.2}$), in apparent tension with the high dynamical mass ($(1.5–3) \times 10^{11} M_\odot$). Detailed analyses of ULIRGs at $z \sim 2$ with photometric constraints on far-infrared dust emission (e.g., Lo Faro et al. 2017) also found that stellar masses inferred using a Calzetti law are systematically lower because of the smaller amount of reddening at near-infrared wavelengths. Clearly, caution should be exercised when applying a single locally calibrated attenuation law at high redshift. Overall, the results highlight the need for deep (sub-)millimeter measurements to determine bolometric luminosities and provide high-redshift empirical constraints on the dust law/energy balance (e.g., Hodge et al. 2016).

For the remainder of the paper we emphasize discussing the implications of the ALMA-only source 3*MM*-1, which likely represents a population that is absent from all current optical-IRAC selected galaxy studies, is below the nominal detection threshold of deep single-dish sub-mm surveys, and therefore deserves more scrutiny.

4.2. Number Counts

A recent unbiased ALMA 3 mm archival search for continuum sources over 130 independent pointings (Zavala et al. 2018a) enabled the first 3 mm number counts. For archival searches, however, detection limits and effective search area are necessarily very inhomogeneous due to the strong variation of the ALMA primary beam response, complicating a straightforward comparison of results. Restricting the comparison to 3*MM*-1, we apply their best-fit power law to the cumulative number counts, which considers effective selection area and incompleteness, predicting one source brighter than $S_{3mm} > 155 \mu Jy$ per 16^{+16}_{-8} arcmin^2. This is consistent with our finding one source in our effective survey area of 8 arcmin^2 (see Section 2.2).

We note that given the estimated stellar mass of $\sim 10^{10.8} M_\odot$ at $z = 5.5$, we expect 3*MM*-1 to occupy a massive DMH ($\sim 10^{12} M_\odot$) and to be strongly clustered. While our results are dominated by Poissonian uncertainties, this may imply that the uncertainties in published number counts are underestimates. Clustering may affect source counts from studies over very

small areas such as the ASPECS 4.6 arcmin^2 survey in the HUDF (González-López et al. 2019), and even the counts in the multiple pointings of Zavala et al. (2018a), as these observations were generally targeting moderately sized deep fields (COSMOS, CDFS, UDS). Clustering effects may be exacerbated by the fact that dust obscuration preferentially occurs in massive galaxies (Whitaker et al. 2017). We note that our results are unlikely to be biased by the original primary targets, which were all at low redshift ($z \sim 1.5$). Clearly, larger blind surveys are needed to constrain number densities at the bright end.

4.3. Unbiased ALMA 3 mm Selection of High-redshift Galaxies

Simulations of dust-obscured galaxies in the early universe predict 3 mm continuum selection optimizes the sensitivity to DSFGs at redshift $z > 4$ (Casey et al. 2018). Current evidence is still mixed: continuum-detected faint galaxies in the small ultradeep ALMA ASPECS field are at average $\bar{z} = 2.3$ (González-López et al. 2019), while limited ground-based spectroscopic evidence for sources found in wider-area archival data indicates $\bar{z} = 3.1$ (Zavala et al. 2018a). Note, however, that the luminosity of the sources and volume covered could impact the redshift selection function (Strandet et al. 2016; Brisbin et al. 2017), and follow up ground-based spectroscopy in the optical and near-IR is possibly biased against highly obscured sources at $z > 3$, due to the faintness of Lyα, nebular optical lines, and a lack of wavelength coverage >2.4 μm. Overall, the redshifts of the two continuum sources in this study, a probable $z_{CO} = 3.329$ (based on a single CO line and congruous $z_{phot} = 3.25 \pm 0.15$) and $z_{phot} = 5.5 \pm 1.1$ ($\bar{z} = 4.4$), are consistent with 3 mm favoring higher redshifts than the $\bar{z} = 2.2$ typical for 870 μm selected galaxies (Simpson et al. 2014).

A challenge in determining the selection function is the difficulty of identifying counterparts and determining redshifts. Neither of our two 3 mm sources had counterparts in previous deep optical-to-radio selected catalogs, raising some concern for analyses where this is a critical step (e.g., photometric redshifts or spectroscopic follow up in optical/NIR). This is particularly problematic for single-dish sub-mm observations, due to the large beam size, but here we find it to be challenging even with the high spatial resolution FWHM = 2″ and accurate astrometry offered by ALMA. In the case of 3*MM*-2 the source is very close to a bright foreground galaxy (1″3 to the north), which was initially mistaken as the counterpart. The optical/NIR faintness and low resolution of the *Spitzer*/IRAC data caused it to be missing or blended in existing multiwavelength catalogs. In the case of 3*MM*-1 the combination of high redshift and high obscuration resulted in it being extremely faint and undetected at all optical-infrared wavelengths. It is therefore possible that the identification of the highest-redshift galaxies in existing (sub-)mm selected samples is still incomplete. In addition, obtaining spectroscopic redshifts in the optical/NIR is unfeasible for the faintest sources. ALMA spectral scans targeting CO and [C II] are likely the only recourse until other facilities (e.g., *JWST*/NIRSpec, LMT Redshift Search Receiver) become available.

4.4. Comparison to Other "dark" Galaxies

The observed SED of 3*MM*-1 is different from that of other optical/near-IR/IRAC-faint populations. The ALESS survey
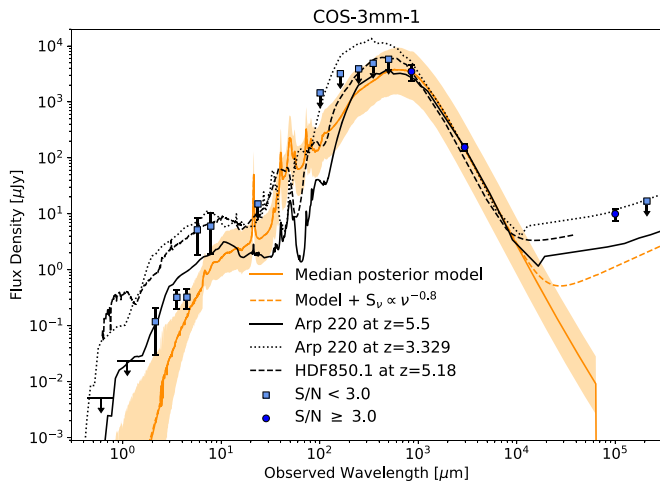
Figure 5. Comparison between the SED of 3*MM*-1 with that of both HDF850.1 and Arp220. The SED-fitting results for 3*MM*-1 are the same as those in the left panel of Figure 4. The SED of Arp220 scaled to the 850 μm and 3 mm photometry of 3*MM*-1, at the photometric redshift of 3*MM*-1, is remarkably similar to the 3*MM*-1 SED. Forcing Arp220 to the redshift of 3*MM*-2 violates the Herschel FIR+sub-mm constraints. The SED of 3*MM*-1 is very similar to that of the bright $z_{\rm spec} = 5.18$ dusty galaxy HDF850.1 (using the SWIRE SED of IRAS 20551-4250 as in Serjeant & Marchetti 2014) scaled to match the average observed 850 μm and 3 mm flux).

identified 9 IRAC-faint SMGs to 1 magnitude brighter IRAC limits (Simpson et al. 2014), but these sources were much brighter in the far-infrared (peaking at 250–350 μm to ∼10 mJy), with a significantly bluer dust peak consistent with $z \sim 2-3$. Such an infrared SED is ruled out by our observations. 3*MM*-1 is fainter at all wavelengths than the so-called H/K−dropout galaxies (e.g., Caputi et al. 2012; Wang et al. 2016; Schreiber et al. 2017), which are generally selected on $H - 4.5$ color, >10× brighter in IRAC, and estimated to be at lower redshift $\bar{z} = 3.7$.

More recently, SCUBA surveys have been carried out to unprecedented depth over CANDELS fields (∼1.5 mJy detection limit; e.g., Cowie et al. 2017, 2018; Koprowski et al. 2017; Zavala et al. 2017; Simpson et al. 2019). Such surveys are deep enough to discover $S_{870} = 2-4$ mJy objects like 3*MM*-1 at $z > 4$. Indeed, the deepest SCUBA surveys have reported submillimeter selected objects that are likely at $z > 4$ and that are either extremely faint at optical-IRAC and MIPS wavelengths (Cowie et al. 2018) or likely initially misidentified and determined to be at high redshift based on the long-wavelength IR SED (e.g., Koprowski et al. 2016). With optical-IRAC magnitudes in the range 29–25 AB, no MIPS detection, and only a marginal 3 GHz radio detection, 3*MM*-1-like objects would have likely defied secure identification, and its probable $z = 5-6$ redshift could have only been determined from the IR SED.

More similar are recently reported ALMA 1.2 mm selected sources from the ASAGAO survey (Yamaguchi et al. 2019) in GOODS-S. These sources also lack obvious counterparts at shorter wavelengths, show extremely small $S_{4.5}/S_{1.2\rm mm}$ and S_{24}/S_{850} flux ratios (indicative of high redshift), but are generally fainter $S_{1.2\,\rm mm} = 0.44-0.8$ mJy than 3*MM*-1 ($S_{1.2\,\rm mm} \sim 2.3$). Additional candidates that lack deep multiwavelength ancillary data may exist outside legacy fields (Wardlow et al. 2018).

4.5. Contribution to CSFRD

The fact that 3*MM*-1 was identified in a survey of such small area suggests that similar galaxies are common in the early universe. Using the effective area of 8 arcmin^2 as derived in Section 2.2, our finding implies a source density of $0.13^{+0.30}_{-0.10}$ arcmin^{-2}, an order of magnitude higher than the rare submillimeter-selected starbursts at $z > 4$ (0.01–0.02 arcmin^{-2}; e.g., Danielson et al. 2017; Marrone et al. 2018). If our results are representative, galaxies like 3*MM*-1 could represent the "iceberg under the tip" of the known extreme dust-obscured star-forming galaxies in the early universe.

Estimating the space densities and contribution to the CSFRD requires estimating a selection volume, which is difficult as we do not know the expected properties or true abundance of DSFGs at $z > 4$. Instead, we derive a simple estimate based on the derived properties of 3*MM*-1. Encouraged by the strong redshift constraints from the long-wavelength photometry, we set the lower bound of the selection volume to the lower 10th percentile redshift probability ($z > 4.1$). The upper bound is chosen to be the redshift beyond which we expect only 0.1 halos of sufficient mass based on the cumulative halo mass function. Using the halo mass function calculator HMF published by Murray et al. (2013) and assuming the halo mass function of Behroozi et al. (2013b) and a high 30% baryon conversion into stars and (converting $M^* = 10^{10.8}M_\odot$ into a conservative $M_{\rm halo} \sim 10^{12}M_\odot$) we compute this upper bound to be $z = 5.7$.

Using this selection volume we determine a space density of $2.9^{+6.5}_{-2.4} \times 10^{-5}$ Mpc^{-3}. We find that the contribution to the CSFRD by 3*MM*-1 is $\rho_{\rm SFR}$ $0.9^{+2.0}_{-0.7} \times 10^{-2}$ $M_\odot$ yr^{-1} Mpc^{-3} (converted to a Chabrier 2003 IMF for comparison with literature measurements). Assuming instead the cumulative space density of massive halos ($>10^{12}$) at $z \sim 5$ using the Behroozi et al. (2013b) halo function, produces a very similar $\rho_{\rm SFR}$ 0.6×10^{-2} $M_\odot$ yr^{-1} Mpc^{-3} for our derived SFR.

With only a single object, the Poissonian uncertainty is large and dominant (Gehrels 1986). Cosmic variance is only on the order of ∼30% based on the calculator by Trenti & Stiavelli (2008), and is therefore not further included. No completeness corrections are applied, because the true distribution is unknown. Figure 6 shows comparisons to various results at $0 < z < 10$ from literature that report dust-uncorrected UV-derived SFR and the dust-obscured SFR (IR-to-millimeter derived).

The contribution of 3*MM*-1 is higher than inferred for the two near-infrared dark ALMA 1.2 mm sources in Yamaguchi et al. (2019), mostly owing to their smaller implied total infrared luminosities. This study does not report formal uncertainties or derive redshifts, which prohibits a more quantitative comparison. Bright SMGs beyond $z > 4$ contribute ∼1×10^{-3} $M_\odot$ yr^{-1} Mpc^{-3} (Swinbank et al. 2014; Michałowski et al. 2017), about an order or magnitude lower than our best estimate. Results from fainter SMGs found in the deepest SCUBA surveys, with luminosities similar to 3*MM*-1 (e.g., Koprowski et al. 2017; Cowie et al. 2018), show a declining contribution at $2 < z < 5$, consistent with our estimates.

Interestingly, if 3*MM*-1 is representative, a population with similar properties could contribute as much to the CSFRD as all known ultraviolet-selected galaxies at similar redshifts combined. This could even imply that dust-obscured star formation continues to dominate the cosmic star formation history beyond $z > 4$, where current infrared-to-mm measurements are incomplete.
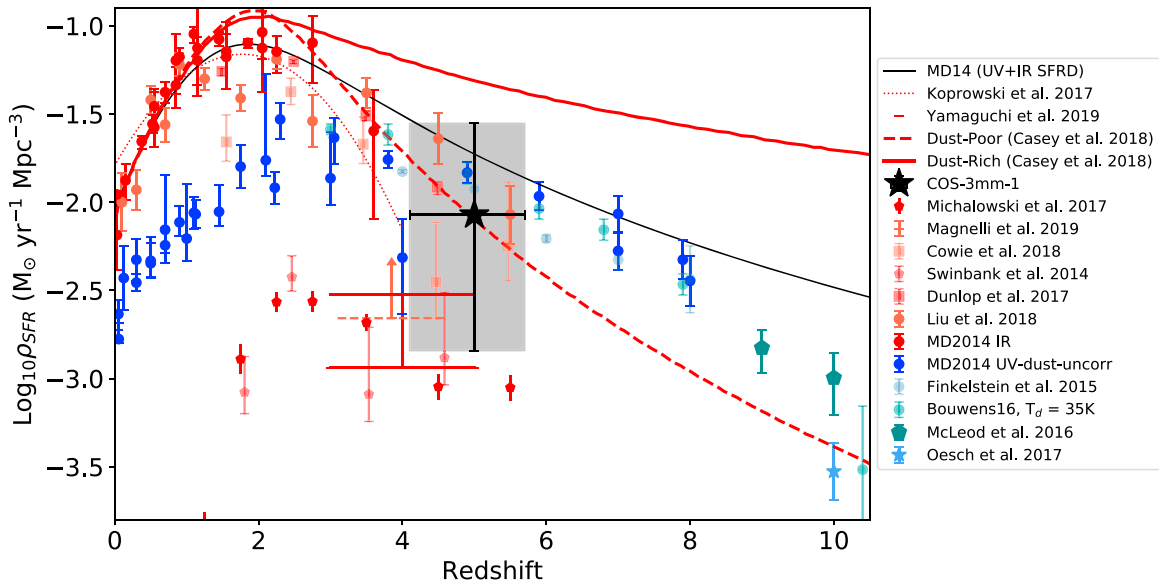
Figure 6. The cosmic star formation history of the universe. Blue shades are UV (dust uncorrected) and red shades are IR-to-millimeter derived SFRs. We add to the compilation of Madau & Dickinson (2014; blue circles) more recent $z > 4$ measurements by Finkelstein et al. (2015), Bouwens et al. (2016), McLeod et al. (2016), and Oesch et al. (2018). Red circles are the dust-obscured IR compilation of Madau & Dickinson (2014), to which we add recent $z > 2$ measurements from Swinbank et al. (2014), Koprowski et al. (2017), Magnelli et al. (2019), Cowie et al. (2018), Dunlop et al. (2017), and Liu et al. (2018). The contribution of 3*MM*-1 is indicated by the black star and shaded region, where the redshift range indicates the estimated selection volume as discussed in Section 4.5.

4.6. Contribution to Stellar Mass Density

The high stellar mass $10^{10.8}\ M_\odot$ and large space density $\sim 3 \times 10^{-5}\ \mathrm{Mpc}^{-3}$ of 3*MM*-1 imply a considerable cosmic stellar mass density (CSMD) in similar objects at $z \sim 5$: $\rho^* = 1.9^{+4.4}_{-1.5} \times 10^6\ M_\odot\,\mathrm{Mpc}^{-3}$, higher than reported for bright ($S_{850} > 4$ mJy) submillimeter galaxies ($\approx 0.5 \times 10^6\ M_\odot\,\mathrm{Mpc}^{-3}$; Michałowski et al. 2017). Comparing to the estimate of the CSMD based on *HST*-selected galaxies $\rho^*(z = 5) = 6.3 \times 10^6 M_\odot\,\mathrm{Mpc}^{-3}$ (Song et al. 2016), suggests that they could contribute a significant fraction ($22^{+25}_{-16}\%$) to the total and perhaps even dominate the high-mass end. The high-mass end of the galaxy stellar mass function at high redshift $z > 4$ is still uncertain and susceptible to biases. Current estimates for the number density of $\sim 10^{10.8}\ M_\odot$ galaxies at $z \sim 5$ are $(1-5) \times 10^{-5}\ \mathrm{Mpc}^{-3}\mathrm{dex}^{-1}$ (Duncan et al. 2014; Grazian et al. 2015; Song et al. 2016; Davidzon et al. 2017; Stefanon et al. 2017), comparable to the space density derived for our ALMA-only galaxy 3*MM*-1. Given that optical-IRAC dark galaxies are missing from these previous studies, it is therefore possible that about half the stellar mass density in high-mass galaxies at $z \sim 5$ remains unaccounted for.

4.7. Implications for the Formation of Massive Galaxies

Bright submillimeter-selected galaxies at $z > 3$ with SFR $\gtrsim 1000\ M_\odot\,\mathrm{yr}^{-1}$ are often hypothesized to be progenitors of massive $z \sim 2$ quiescent galaxies (e.g., Toft et al. 2014; Spilker et al. 2018). More recently, massive quiescent galaxies have been spectroscopically confirmed at $3 < z < 4$ (Glazebrook et al. 2017; Schreiber et al. 2018), but finding their progenitors at even earlier times is challenging. Generally, UV-selected galaxies at $z > 4$ are presumed to not be abundant, massive, and star-forming enough to produce the population of the earliest known massive quiescent galaxies with $N \sim (3-5) \times 10^{-5}\ \mathrm{Mpc}^{-3}$ and Log $(M/M_\odot) \gtrsim 10.6$ (Straatman et al. 2014).

Bright (>4 mJy) submillimeter galaxies are a possible avenue, but it is difficult to establish a conclusive connection. Estimated SMG number densities at $z > 4$ are low and uncertain $\sim 0.1-3 \times 10^{-6}\ \mathrm{Mpc}^{-3}$ (Ivison et al. 2016; Michałowski et al. 2017; Jin et al. 2018). While their high SFRs indicate they will rapidly form massive galaxies, the modest inferred gas masses indicate gas depletion timescales on the order of 10–100 Myr (e.g., Aravena et al. 2016; Spilker et al. 2018), and large duty cycle corrections are needed to make up for the low number densities.

The inferred space densities and stellar mass of 3*MM*-1, on the other hand, are already as large as those reported for the population of early quiescent galaxies at $3 < z < 4$ (Nayyeri et al. 2014; Straatman et al. 2014). The large $\sim 10^{11} M_\odot$ gas mass and modest SFR indicates much longer depletion timescales ($\sim 200-500$ Myr), half the age of the universe at this epoch, and implies a $\sim 50\%-100\%$ duty cycle for our adopted $4 \lesssim z \lesssim 6$ selection window. 3*MM*-1 could therefore represent a more gradual path for massive galaxy growth compared to a rapid and bursty formation, as has been found in some bright merger-induced SMGs (e.g., Marrone et al. 2018; Pavesi et al. 2018). Overall, our results provide evidence for the existence of a sustained growth mode for massive galaxies in the early universe.

Finally, the large systematic difference in SFR and stellar mass in particular depending on the assumed attenuation model for 3*MM*-2 suggests exercising caution when relating progenitors and descendants galaxies. Often, such links are determined based on the capability of a progenitor population to produce adequate numbers of sufficiently massive galaxies at later times (e.g., Straatman et al. 2014; Toft et al. 2014; Williams et al. 2014, 2015), or by the assumption that the rank-order on stellar mass can be reliably determined (e.g., Brammer et al. 2011; Behroozi et al. 2013a; Leja et al. 2013). Such determinations could be more uncertain than has been accounted for if the derived stellar masses of individual galaxies are off by factors

of ~ 8 (see Section 3.2). This is a particular concern at high redshift $z > 3$, where very few galaxies have high enough S/N (sub-)millimeter observations for meaningful constraints on the dust attenuation model. These results are obviously based on only a single galaxy and larger samples with full optical-to-millimeter photometry are needed to determine the scatter in stellar mass.

4.8. Future ALMA and JWST Observations

The dark nature of the 3*MM*-1 non-detection in very deep stacked optical and near-IR data, and the faint IRAC fluxes, suggest a prominent population of DSFGs at $z > 4$. The high inferred redshift may point to the efficacy of blind surveys at 2–3 mm at finding the earliest dusty star-forming galaxies (Béthermin et al. 2015; Casey et al. 2018). These galaxies are below the classical detection limit (>4 mJy) of bright galaxies found in single-dish submillimeter surveys. Deep 2 mm single-dish and wider 1–3 mm ALMA (sub)-millimeter surveys are only just starting to push into this territory at very high redshift (e.g., Magnelli et al. 2019; Yamaguchi et al. 2019). Until the launch of the *James Webb Space Telescope* (*JWST*), ALMA alone can find and study these galaxies.

Wide-area unbiased ALMA surveys covering hundreds of arcmin^2 are necessary to further constrain their prominence in the early universe. Such surveys are feasible at 2–3 mm with ALMA because of the relatively large size of the primary ALMA beam and the exquisite sensitivity to high-redshift star-forming galaxies even in short integration times (Casey et al. 2019). To date, none of the ALMA-only galaxies found have been spectroscopically confirmed, but spectral line scans for CO and in particular [C II] are efficient and feasible with ALMA. Future surveys with *JWST* will enable systematic studies of large samples of faint SMG galaxies. Large legacy surveys such as the *JWST* Advanced Deep Extragalactic Survey (JADES) will likely characterize ~ 15–30 galaxies similar to 3*MM*-1 (based on expected number densities from this work and Zavala et al. 2018a, and observations described in Williams et al. 2018). *JWST* will have the capability to measure stellar population properties and redshifts, and in combination with ALMA far-infrared constraints, will enable a detailed investigation into the star formation, dust, and stellar population properties of massive galaxies in the early universe.

Appendix

Here we present supplemental observational details for 3*MM*-1 and 3*MM*-2. In Table 2, we present the deblended photometry (measurements and 1σ uncertainties) based on the ALMA priors for the two 3-mm sources that are used in the SED-fitting analysis presented in Section 2.4. In Figures 7 and 8 we present the posterior probability distributions for the galaxy properties of both sources measured using the Bayesian SED fitting with BAGPIPES.

Table 2
ALMA Prior-based Deblended Photometry

Band	3*MM*-1 flux density (μJy)	rms	3*MM*-2 flux density (μJy)	rms
SUBARU B	[−1.3E−02]	7.8E−03	⋯	⋯
HSC g	[3.6E−03]	1.5E−02	[2.3E−02]	1.1E−02
SUBARU V	[−7.6E−03]	1.8E−02	⋯	⋯
HSC r	[−1.2E−02]	1.4E−02	9.3E−02	9.7E−03
SUBARU rp	[1.2E−03]	1.7E−02	⋯	⋯
SUBARU ip	[2.0E−03]	2.6E−02	⋯	⋯
HSC i	[−1.0E−02]	2.1E−02	1.2E−01	1.5E−02
HSC z	[1.2E−02]	3.0E−02	1.3E−01	2.4E−02
SUBARU zp	[−1.5E−01]	6.5E−02	⋯	⋯
HSC Y	[2.2E−02]	7.4E−02	[4.9E−02]	5.8E−02
UltraVISTA Y	[9.7E−03]	8.9E−02	[1.6E−01]	8.2E−02
UltraVISTA J	[−1.1E−01]	1.0E−01	[2.0E−01]	8.9E−02
UltraVISTA H	[−5.9E−02]	1.3E−01	6.3E−01	1.1E−01
UltraVISTA Ks	[1.2E−01]	8.8E−02	8.4E−01	8.7E−02
Spitzer/ IRAC 3.6 μm	[3.2E−01]	1.2E−01	1.7E+00	9.2E−02
Spitzer/ IRAC 4.5 μm	[3.2E−01]	1.3E−01	3.0E+00	9.9E−02
Spitzer/ IRAC 5.8 μm	[5.2E+00]	3.3E+00	8.8E+00	2.2E+00
Spitzer/ IRAC 8 μm	[6.0E+00]	4.1E+00	[7.7E+00]	2.9E+00
Spiter/ MIPS 24 μm	[1.1E+01]	1.5E+01	[2.6E+01]	1.5E+01
Herschel/PACS 100 μm	[7.1E+02]	1.4E+03	[1.5E+02]	1.4E+03
Herschel/PACS 160 μm	[−2.4E+03]	3.2E+03	[−1.9E+03]	3.2E+03
Herschel/SPIRE 250 μm	[3.7E+03]	3.9E+03	[1.0E+03]	3.9E+03
Herschel/SPIRE 350 μm	[4.3E+03]	4.9E+03	[−5.0E+02]	4.9E+03
Herschel/SPIRE 500 μm	[5.5E+03]	5.8E+03	[4.4E+03]	5.8E+03
SCUBA2 850 μm	3.5E+03	1.1E+03	[4.0E+02]	1.1E+03
ALMA 3 mm	1.6E+02	2.2E+01	7.5E+01	1.0E+01
VLA 3 GHz	1.0E+01	2.4E+00	[3.9E+00]	2.4E+00
VLA 1.4 GHz	[1.7E+01]	1.7E+01	[4.0E+01]	1.7E+01

Note. Subaru optical photometry for 3*MM*-2 are not measured owing to cosmetic defects in the mosaics that cross the location of the source. Photometric upper limits as indicated by downward arrows in Figure 4 are at the rms values of photometric points in this table where S/N < 1. Non-significant photometric points (with SNR < 3) are indicated with brackets.
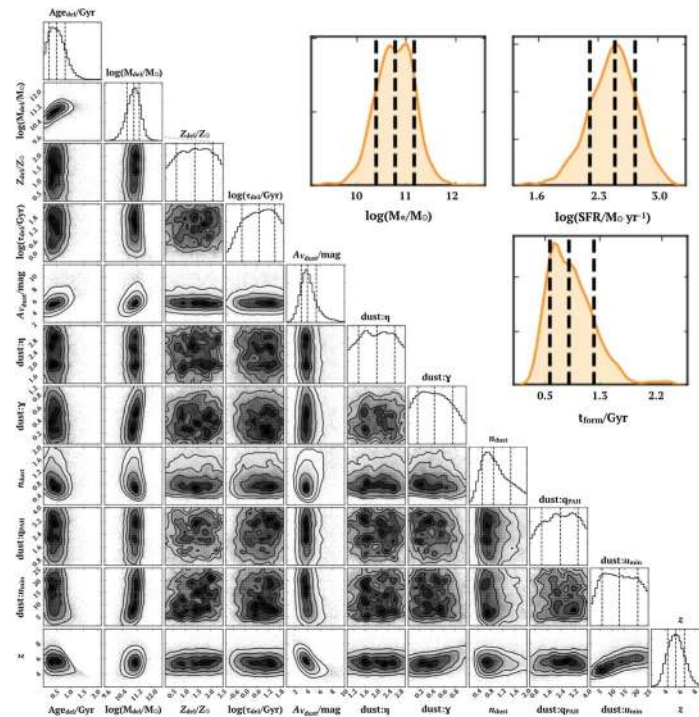
Figure 7. Posterior probability distributions for the fitted parameters of 3*MM*-1 corresponding to the orange region in Figure 4, assuming Charlot & Fall (2000) dust attenuation with the slope left free. M_{del} refers to the total stars formed (integral of the delayed star formation history), whereas M^* is the stellar mass excluding remnants and including mass loss due to stellar evolution, and is the parameter referred to throughout the text. Parameters, their definitions, and their uncertainties are presented in Table 1.
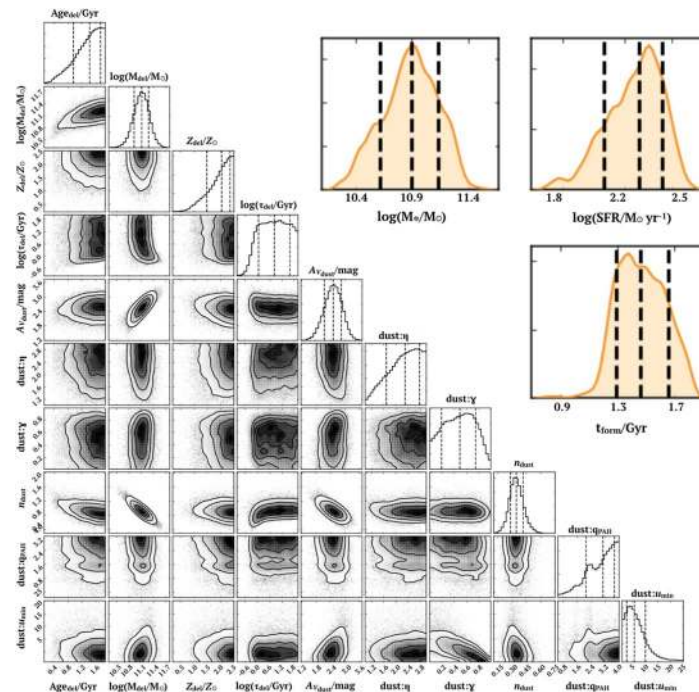

Figure 8. Posterior probability distributions for the fitted parameters of 3*MM*-2 corresponding to the orange region in Figure 4, assuming Charlot & Fall (2000) dust attenuation with the slope left free, and fixed to the spectroscopic redshift. Measured parameters, their definitions, and their uncertainties are presented in Table 1.

ORCID iDs

Christina C. Williams ⓘ https://orcid.org/0000-0003-2919-7495
Justin Spilker ⓘ https://orcid.org/0000-0003-3256-5615
Mauro Stefanon ⓘ https://orcid.org/0000-0001-7768-5309
Joel Leja ⓘ https://orcid.org/0000-0001-6755-1315

Katherine Whitaker ⓘ https://orcid.org/0000-0001-7160-3632
Rachel Bezanson ⓘ https://orcid.org/0000-0001-5063-8254
Desika Narayanan ⓘ https://orcid.org/0000-0002-7064-4309
Pascal Oesch ⓘ https://orcid.org/0000-0001-5851-6649
Benjamin Weiner ⓘ https://orcid.org/0000-0001-6065-7483

References

Aihara, H., Arimoto, N., Armstrong, R., et al. 2018a, PASJ, 70, S4
Aihara, H., Armstrong, R., Bickerton, S., et al. 2018b, PASJ, 70, S8
Aravena, M., Decarli, R., Walter, F., et al. 2016, ApJ, 833, 68
Aretxaga, I., Wilson, G. W., Aguilar, E., et al. 2011, MNRAS, 415, 3831
Behroozi, P. S., Marchesini, D., Wechsler, R. H., et al. 2013a, ApJL, 777, L10
Behroozi, P. S., Wechsler, R. H., & Conroy, C. 2013b, ApJ, 770, 57
Béthermin, M., De Breuck, C., Sargent, M., & Daddi, E. 2015, A&A, 576, L9
Bezanson, R., Spilker, J., Williams, C. C., et al. 2019, ApJL, 873, L19
Bothwell, M. S., Smail, I., Chapman, S. C., et al. 2013, MNRAS, 429, 3047
Bouwens, R. J., Oesch, P. A., Labbé, I., et al. 2016, ApJ, 830, 67
Brammer, G. B., Whitaker, K. E., van Dokkum, P. G., et al. 2011, ApJ, 739, 24
Brisbin, D., Miettinen, O., Aravena, M., et al. 2017, A&A, 608, A15
Bruzual, G., & Charlot, S. 2003, MNRAS, 344, 1000
Byler, N., Dalcanton, J. J., Conroy, C., & Johnson, B. D. 2017, ApJ, 840, 44
Calzetti, D., Armus, L., Bohlin, R. C., et al. 2000, ApJ, 533, 682
Caputi, K. I., Dunlop, J. S., McLure, R. J., et al. 2012, ApJL, 750, L20
Carilli, C. L., & Yun, M. S. 1999, ApJL, 513, L13
Carnall, A. C., Leja, J., Johnson, B. D., et al. 2019, ApJ, 873, 44
Carnall, A. C., McLure, R. J., Dunlop, J. S., & Davé, R. 2018, MNRAS, 480, 4379
Casey, C. M., Capak, P., Staguhn, J., et al. 2019, BAAS, 51, 212
Casey, C. M., Hodge, J., Zavala, J., et al. 2018, ApJ, 862, 78
Casey, C. M., Narayanan, D., & Cooray, A. 2014, PhR, 541, 45
Chabrier, G. 2003, PASP, 115, 763
Charlot, S., & Fall, M. 2000, ApJ, 539, 718
Chevallard, J., Charlot, S., Wandelt, B., & Wild, V. 2013, MNRAS, 432, 2061
Civano, F., Marchesi, S., Comastri, A., et al. 2016, ApJ, 819, 62
Cooray, A., Calanog, J., Wardlow, J. L., et al. 2014, ApJ, 790, 40
Cowie, L. L., Barger, A. J., Hsu, L.-Y., et al. 2017, ApJ, 837, 139
Cowie, L. L., González-López, J., Barger, A. J., et al. 2018, ApJ, 865, 106
da Cunha, E., Walter, F., Smail, I. R., et al. 2015, ApJ, 806, 110
Daddi, E., Dannerbauer, H., Stern, D., et al. 2009, ApJ, 694, 1517
Danielson, A. L. R., Swinbank, A. M., Smail, I., et al. 2017, ApJ, 840, 78
Davidzon, I., Ilbert, O., Laigle, C., et al. 2017, A&A, 605, A70
Delhaize, J., Smolčić, V., Delvecchio, I., et al. 2017, A&A, 602, A4
Draine, B. T., & Li, A. 2007, ApJ, 657, 810
Duncan, K., Conselice, C. J., Mortlock, A., et al. 2014, MNRAS, 444, 2960
Dunlop, J. S., McLure, R. J., Biggs, A. D., et al. 2017, MNRAS, 466, 861
Dunlop, J. S., McLure, R. J., Yamada, T., et al. 2004, MNRAS, 350, 769
Ferland, G. J., Chatzikos, M., Guzmán, F., et al. 2017, RMxAA, 53, 385
Finkelstein, S. L., Ryan, R. E., Jr., Papovich, C., et al. 2015, ApJ, 810, 71
Franco, M., Elbaz, D., Béthermin, M., et al. 2018, A&A, 620, A152
Geach, J. E., Dunlop, J. S., Halpern, M., et al. 2017, MNRAS, 465, 1789
Gehrels, N. 1986, ApJ, 303, 336
Glazebrook, K., Schreiber, C., Labbé, I., et al. 2017, Natur, 544, 71
González-López, J., Decarli, R., Pavesi, R., et al. 2019, ApJ, 882, 139
Grazian, A., Fontana, A., Santini, P., et al. 2015, A&A, 575, A96
Hatsukade, B., Kohno, K., Yamaguchi, Y., et al. 2018, PASJ, 70, 105
Hodge, J. A., Swinbank, A. M., Simpson, J. M., et al. 2016, ApJ, 833, 103
Hurley, P. D., Oliver, S., Betancourt, M., et al. 2017, MNRAS, 464, 885
Ivison, R. J., Lewis, A. J. R., Weiss, A., et al. 2016, ApJ, 832, 78
Jin, S., Daddi, E., Liu, D., et al. 2018, ApJ, 864, 56
Kennicutt, R. C., & Evans, N. J. 2012, ARA&A, 50, 531
Kennicutt, R. C., Jr. 1998, ApJ, 498, 541
Kirkpatrick, A., Pope, A., Sajina, A., et al. 2015, ApJ, 814, 9
Koekemoer, A. M., Aussel, H., Calzetti, D., et al. 2007, ApJS, 172, 196
Koprowski, M. P., Dunlop, J. S., Michałowski, M. J., et al. 2016, MNRAS, 458, 4321
Koprowski, M. P., Dunlop, J. S., Michałowski, M. J., et al. 2017, MNRAS, 471, 4155
Kroupa, P. 2001, MNRAS, 322, 231
Labbé, I., Oesch, P. A., Bouwens, R. J., et al. 2013, ApJL, 777, L19
Labbé, I., Oesch, P. A., Illingworth, G. D., et al. 2015, ApJS, 221, 23
Laigle, C., McCracken, H. J., Ilbert, O., et al. 2016, ApJS, 224, 24
Le Floc'h, E., Aussel, H., Ilbert, O., et al. 2009, ApJ, 703, 222

Leja, J., Carnall, A. C., Johnson, B. D., Conroy, C., & Speagle, J. S. 2019, ApJ, 876, 3
Leja, J., Johnson, B. D., Conroy, C., & van Dokkum, P. 2018, ApJ, 854, 62
Leja, J., Johnson, B. D., Conroy, C., van Dokkum, P. G., & Byler, N. 2017, ApJ, 837, 170
Leja, J., van Dokkum, P., & Franx, M. 2013, ApJ, 766, 33
Liu, D., Daddi, E., Dickinson, M., et al. 2018, ApJ, 853, 172
Lo Faro, B., Buat, V., Roehlly, Y., et al. 2017, MNRAS, 472, 1372
Madau, P., & Dickinson, M. 2014, ARA&A, 52, 415
Magnelli, B., Ivison, R. J., Lutz, D., et al. 2015, A&A, 573, A45
Magnelli, B., Karim, A., Staguhn, J., et al. 2019, ApJ, 877, 45
Marrone, D. P., Spilker, J. S., Hayward, C. C., et al. 2018, Natur, 553, 51
McCracken, H. J., Milvang-Jensen, B., Dunlop, J., et al. 2012, A&A, 544, A156
McLeod, D. J., McLure, R. J., & Dunlop, J. S. 2016, MNRAS, 459, 3812
Michałowski, M. J., Dunlop, J. S., Koprowski, M. P., et al. 2017, MNRAS, 469, 492
Murray, S. G., Power, C., & Robotham, A. S. G. 2013, MNRAS, 434, L61
Muzzin, A., Marchesini, D., Stefanon, M., et al. 2013, ApJS, 206, 8
Narayanan, D., Conroy, C., Davé, R., Johnson, B. D., & Popping, G. 2018, ApJ, 869, 70
Narayanan, D., & Krumholz, M. R. 2014, MNRAS, 442, 1411
Nayyeri, H., Mobasher, B., Hemmati, S., et al. 2014, ApJ, 794, 68
Oesch, P. A., Bouwens, R. J., Illingworth, G. D., Labbé, I., & Stefanon, M. 2018, ApJ, 855, 105
Oliver, S. J., Bock, J., Altieri, B., et al. 2012, MNRAS, 424, 1614
Pavesi, R., Riechers, D. A., Sharon, C. E., et al. 2018, ApJ, 861, 43
Salim, S., Boquien, M., & Lee, J. C. 2018, ApJ, 859, 11
Salmon, B., Papovich, C., Long, J., et al. 2016, ApJ, 827, 20
Sanders, D. B., Salvato, M., Aussel, H., et al. 2007, ApJS, 172, 86
Schinnerer, E., Sargent, M. T., Bondi, M., et al. 2010, ApJS, 188, 384
Schinnerer, E., Smolčić, V., Carilli, C. L., et al. 2007, ApJS, 172, 46
Schreiber, C., Glazebrook, K., Nanayakkara, T., et al. 2018, A&A, 618, A85
Schreiber, C., Pannella, M., Leiton, R., et al. 2017, A&A, 599, A134
Scoville, N., Sheth, K., Aussel, H., et al. 2016, ApJ, 820, 83
Serjeant, S., & Marchetti, L. 2014, MNRAS, 443, 3118
Silverman, J. D., Rujopakarn, W., Daddi, E., et al. 2018, ApJ, 867, 92
Simpson, J. M., Smail, I., Swinbank, A. M., et al. 2019, ApJ, 880, 43
Simpson, J. M., Swinbank, A. M., Smail, I., et al. 2014, ApJ, 788, 125
Smolčić, V., Novak, M., Bondi, M., et al. 2017, A&A, 602, A1
Song, M., Finkelstein, S. L., Ashby, M. L. N., et al. 2016, ApJ, 825, 5
Spilker, J. S., Aravena, M., Béthermin, M., et al. 2018, Sci, 361, 1016
Spilker, J. S., Marrone, D. P., Aravena, M., et al. 2016, ApJ, 826, 112
Stefanon, M., Bouwens, R. J., Labbé, I., et al. 2017, ApJ, 843, 36
Straatman, C. M. S., Labbé, I., Spitler, L. R., et al. 2014, ApJL, 783, L14
Strandet, M. L., Weiss, A., De Breuck, C., et al. 2017, ApJL, 842, L15
Strandet, M. L., Weiss, A., Vieira, J. D., et al. 2016, ApJ, 822, 80
Swinbank, A. M., Simpson, J. M., Smail, I., et al. 2014, MNRAS, 438, 1267
Taniguchi, Y., Scoville, N., Murayama, T., et al. 2007, ApJS, 172, 9
Tisanić, K., Smolčić, V., Delhaize, J., et al. 2019, A&A, 621, A139
Toft, S., Smolčić, V., Magnelli, B., et al. 2014, ApJ, 782, 68
Trenti, M., & Stiavelli, M. 2008, ApJ, 676, 767
van der Wel, A., Franx, M., van Dokkum, P. G., et al. 2014, ApJ, 788, 28
Walter, F., Decarli, R., Carilli, C., et al. 2012, Natur, 486, 233
Wang, R., Wagg, J., Carilli, C. L., et al. 2013, ApJ, 773, 44
Wang, T., Elbaz, D., Schreiber, C., et al. 2016, ApJ, 816, 84
Wardlow, J. L., Simpson, J. M., Smail, I., et al. 2018, MNRAS, 479, 3879
Weiß, A., Kovács, A., Coppin, K., et al. 2009, ApJ, 707, 1201
Whitaker, K. E., Pope, A., Cybulski, R., et al. 2017, ApJ, 850, 208
Williams, C. C., Curtis-Lake, E., Hainline, K. N., et al. 2018, ApJS, 236, 33
Williams, C. C., Giavalisco, M., Cassata, P., et al. 2014, ApJ, 780, 1
Williams, C. C., Giavalisco, M., Lee, B., et al. 2015, ApJ, 800, 21
Wuyts, S., Förster Schreiber, N. M., Lutz, D., et al. 2011, ApJ, 738, 106
Yamaguchi, Y., Kohno, K., Hatsukade, B., et al. 2019, ApJ, 878, 73
Zavala, J. A., Aretxaga, I., Geach, J. E., et al. 2017, MNRAS, 464, 3369
Zavala, J. A., Casey, C. M., da Cunha, E., et al. 2018a, ApJ, 869, 71
Zavala, J. A., Montaña, A., Hughes, D. H., et al. 2018b, NatAs, 2, 56